J Adv Ceram

Research Article

Composite powder design strategy enabling vat photopolymerization 3D printing of lithium disilicate glass-ceramics with high precision, strength, and antibacterial properties

Fan Zhang[1], Yujun Zhang[2], Junfeng Kang[3], Shouren Wang[1], Zhen Xiao[1], Xiuli Fu[1], Gaoqi Wang[1,✉]

Cite this article: Zhang F, Zhang Y, Kang J, et al. *J Adv Ceram* 2026, **15**(3): 9221253. https://doi.org/10.26599/JAC.2026.9221253

ABSTRACT: Lithium disilicate glass-ceramic is a widely used dental restoration material valued for its aesthetic semitranslucency, high strength, and excellent biocompatibility. Vat photopolymerization, a form of three-dimensional (3D) printing, presents a transformative alternative to the conventional powder sintering and machining of this material, offering significant improvements in production efficiency and material utilization. However, 3D printing lithium disilicate glass-ceramics is challenging, primarily due to severe light scattering caused by their high transparency, which compromises printing accuracy. This study proposes a functional composite powder design strategy that incorporates carbon and zinc oxide powders into a lithium disilicate matrix based on light scattering principles. Through optical simulations and experimental validation, the composition was rationally optimized to produce functional dental prostheses with high precision, strength, and antibacterial properties. Carbon confines light scattering via its high extinction coefficient, and zinc oxide secures an adequate curing depth via its high refractive index, synergistically ensuring high precision. This work lays a foundation for advancing the 3D printing and clinical application of functional lithium disilicate glass-ceramics.

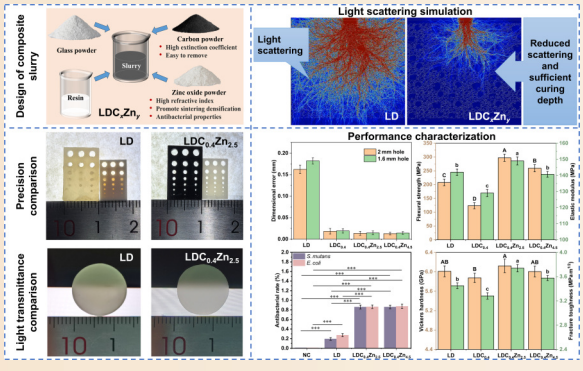

KEYWORDS: lithium disilicate glass-ceramic; forming accuracy; mechanical properties; antibacterial property; digital light processing

1 Introduction

Lithium disilicate glass-ceramic has been widely used in dental restorations owing to its high mechanical strength, tooth-like translucency, and excellent biocompatibility [1–5]. The conventional manufacturing technique for lithium disilicate glass-ceramics, which involves powder sintering followed by machining, presents limitations such as complex manufacturing processes, prolonged production cycles, and high material consumption. These drawbacks make it challenging to fabricate samples with high precision and complex geometries [6,7]. Ceramic three-dimensional (3D) printing technology constructs three-dimensional solid objects through a layer-by-layer material deposition process. It is characterized by high forming accuracy, excellent surface quality, and high printing efficiency, leading to its extensive application in fields such as aerospace and biomedical engineering [8–11]. Among various ceramic 3D printing technologies, photopolymerization-based techniques (including digital light processing (DLP) and stereolithography (SLA)) are widely used and extensively researched [8,10,12,13]. However, the high translucency and refractive index mismatch between the resin and the glass powders induce substantial scattering of the curing light, which in turn severely compromises the printing accuracy in photopolymerization-based 3D printing processes [14–16]. Dental restorations often incorporate intricate internal structures (e.g., the internal channels of root canal posts and implant abutments) and delicate surface textures. Furthermore, restorations such as crowns, inlays, and veneers require high-precision matching with residual tooth structures or adjacent teeth within the oral cavity. Inadequate restoration accuracy can not only lead to dimensional mismatches between the restoration and the tooth preparation but may also allow bacteria to infiltrate the

[1] Shandong Key Laboratory of Surface Engineering and Intelligent Equipment for Key Metal Components, School of Mechanical Engineering, University of Jinan, Jinan 250022, China. [2] Department of Prosthodontics, School and Hospital of Stomatology, Cheeloo College of Medicine, Shandong University, Jinan 250012, China. [3] School of Materials Science and Engineering, University of Jinan, Jinan 250002, China.

✉ Corresponding author. E-mail: me_wanggq@ujn.edu.cn

Received: October 12, 2025; Revised: December 18, 2025; Accepted: January 17, 2026

resulting gaps, potentially causing secondary caries and other diseases [17].

Currently, the primary strategies for improving the printing accuracy of photopolymerization-based additive manufacturing for transparent and semitransparent materials mainly involve optimizing process parameters, improving the rheological properties of ceramic suspensions, and modifying the refractive index of the powder [18–20]. However, approaches such as optimizing process parameters and improving the rheological properties of ceramic suspensions often yield only marginal improvements in printing accuracy. Modifying the refractive index, in contrast, offers a more effective pathway to enhance printing precision. For instance, Chen *et al.* [14] improved the printing accuracy of silicon nitride by coating the powder to achieve better refractive index matching with the photocurable resin. Although effective, this method typically entails rather intricate processing steps and may introduce challenges in completely removing the coating material.

The key optical parameters governing this process are the refractive index and the extinction coefficient, with the latter defining a material's ability to absorb light. Adjusting the extinction coefficient of the ceramic slurry also represents an effective strategy for improving printing accuracy. A higher extinction coefficient results in stronger absorption of excess scattered light and a reduced penetration depth. This confinement of the light to the intended exposure area minimizes stray light in nonprinting regions, thereby enhancing forming accuracy. He *et al.* [21] incorporated a novel photoinhibitor (curcumin–Na (Cur–Na)) into cell-laden hydrogels to mitigate light scattering, which successfully improved printing resolution. In our previous work [22], zirconia with a high extinction coefficient was doped into a fluorapatite glass powder slurry to reduce light transmittance, effectively restricting the light to a smaller area and significantly improving printing accuracy. However, a critical limitation is that zirconia cannot be removed in subsequent processing steps, which adversely affects the final transparency of the glass-ceramic. Qian *et al.* [15] added carbon (C) powder to silica slurry to reduce light scattering, addressing the overpolymerization issue caused by silica's high optical transparency. C powder is a material with a relatively high extinction coefficient. Although intrinsically black, C can be completely oxidized into carbon dioxide and volatilized during the sintering process. This allows it to function as a temporary absorber without introducing residual impurities that would compromise the color and semitranslucency of the final dental prosthesis. However, the high extinction coefficient of C powder leads to excessive absorption of light, which attenuates the propagation of light energy into the deeper layers of the slurry. This results in an insufficient curing depth, thereby weakening the interlayer bonding strength and mechanical properties. Therefore, another particle with a low extinction coefficient and an appropriate refractive index can be added to buffer the excessively high extinction coefficient of the C powder, thereby mitigating the insufficient curing depth.

This effect will thereby increase the curing depth and improve interlayer bonding as well as printing quality. Zinc oxide (ZnO) is a material with a low extinction coefficient and a refractive index close to that of the resin. The low extinction coefficient of ZnO helps reduce excessive light absorption in the C-containing composite slurry. Moreover, its matching refractive index minimizes the mismatch between the resin and the composite powders, thereby suppressing lateral light scattering and promoting longitudinal propagation of light. Moreover, ZnO has been proven to have excellent antibacterial properties [23–26]. Micrometer-sized gaps at the restoration–tooth interface allow the infiltration of bacteria and their acidic metabolites, leading to secondary caries, peri-implantitis, and ultimately, implant failure [17]. Therefore, endowing dental restorations with antibacterial properties is crucial for their long-term clinical success in the oral environment [26]. Current strategies to achieve this goal mainly involve incorporating pharmaceutical agents or metal oxides [27,28]. Among them, metal oxides are preferred for ceramic materials due to their broad-spectrum efficacy and low risk of inducing bacterial resistance. ZnO stands out for its high chemical stability, cost-effectiveness, aesthetic compatibility, and photocatalytic activity, making it an optimal functional component. In summary, the introduction of ZnO can not only improve the light curing depth and forming quality through optical regulatory mechanisms but also endow the restoration with antibacterial functionality.

Therefore, this study proposes a composite powder design strategy for fabricating functional lithium disilicate composites via 3D printing. First, optical simulations of the photopolymerization process were performed to elucidate the light scattering behavior within the slurry containing lithium disilicate, C, and ZnO, with the component ratios being preliminarily optimized based on the simulation results. Subsequently, the effects of these components on the printing accuracy, microstructure, and mechanical properties of the glass-ceramics were systematically investigated. Finally, the antibacterial efficacy imparted by ZnO was quantitatively assessed through standard antibacterial tests.

2 Experimental design and methods

2.1 Design method of functional lithium silicate composites

The mismatch in refractive indices between lithium silicate glass powder and the photosensitive resin led to significant light scattering, causing the light to propagate along random and dispersed paths. Since both materials exhibited low absorption coefficients, most of this scattered light was not absorbed in a timely manner. To address this, C was introduced for its high extinction coefficient, which enabled rapid absorption of the scattered light. However, the strong absorption by C necessitated higher exposure energy to achieve the required curing depth. This drawback could be offset by incorporating ZnO, which not only mitigates the limitations posed by C but also imparted antibacterial functionality. Consequently, a lithium silicate/C/ZnO composite material was designed, with the curing accuracy, mechanical performance, and antibacterial efficacy serving as the key criteria for optimizing the material composition.

The light scattering characteristics, including its width and depth, were obtained through numerical simulations performed with ANSYS Lumerical software, which solved Maxwell's equations using the finite element method. The optical parameters were set based on previous studies and official documentation [15,22,29–32]. The refractive indices of the resin and the glass-ceramic were selected as 1.456 and 1.6, with extinction coefficients of 0.005 and 0, respectively [15,22,29,30]. The refractive indices of C and ZnO were set to 2.77 and 1.97, with corresponding extinction coefficients of 1.26 and 0.01 [31,32]. Four distinct models were established: (1) unfilled resin; (2) a slurry with 45 vol% solid loading, represented by 490 glass-ceramic particles; (3) a composite slurry with 0.4 wt% C, represented by 490 glass-ceramic and 1350 C particles; (4) a composite slurry with 0.4 wt% C and 2.5 wt% ZnO, represented by 490 glass-ceramic, 1350 C, and 1110 ZnO particles. The model area was a 40 μm × 40 μm,

with a 385 nm wavelength ultraviolet beam incident from its top edge. To represent the actual particle morphologies after ball milling, glass-ceramic particles were modeled as hexagons (1–7 μm in diagonal length), C particles as circles (0.05–0.2 μm in diameter), and ZnO particles as polygons (0.5–1.2 μm in diameter) [22,29,33]. Perfectly matched layer absorption boundary conditions were applied to the left, right, and bottom boundaries of the model, with consistent incident light settings across all simulations.

2.2 3D printing and performance test

2.2.1 *Raw materials*

Nanosized C powder and the initial glass raw materials—including SiO_2, Li_2CO_3, MgO, Al_2O_3, K_2CO_3, Na_2CO_3, $NH_4H_2PO_4$, CaO, ZnO, and ZrO_2—were analytical-grade reagents obtained from Shanghai Macklin Biochemical Technology Co., Ltd., (China). The photosensitive slurry components, including 1,6-hexanediol diacrylate (HDDA), trimethylolpropane triacrylate (TMPTA), dispersant BYK-111, and photoinitiator diphenyl(2,4,6-trimethylbenzoyl)phosphine oxide (TPO), were also procured from the same supplier.

2.2.2 *Preparation of composite powders and slurry*

The preparation and manufacturing process of the functional glass-ceramics is shown in Fig. 1. The lithium disilicate base glass was synthesized using raw materials, and the composition of the base glass comprised 68.62% SiO_2, 13.5% Li_2O, 1.8% MgO, 4.57% Al_2O_3, and 4.18% P_2O_5, along with other trace elements. The mixed raw materials were placed in a quartz crucible, heated to 1550 °C in the furnace, and maintained for 2 h. Then, the molten glass was quenched in deionized water, followed by thorough drying. The dried glass was crushed into base glass powder using a planetary ball mill (KE-2L, Qidong Honghong Instrument and Equipment Factory, China) and sieved through an 800-mesh sieve.

A solid loading of 45 vol% was selected for the ceramic suspension. The lithium disilicate glass powder was dispersed in a premixed solution containing HDDA and TMPTA as the acrylic monomer system. The formulation also included dispersant BYK-111 (5 wt% relative to the powder), photoinitiator TPO (4 wt% relative to the monomers), C powder (0–0.6 wt% relative to the powder), and ZnO (0–4.5 wt% relative to the powder). As shown in Fig. 2, the samples were designated based on their composition. "LD" denoted the pure glass-ceramic without C or ZnO. "LDC_x" represented the LD composition with the addition of x wt% C powder. "LDC_xZn_y" indicated the further addition of y wt% ZnO to the LDC_x composition.

2.2.3 *3D printing and sintering*

The ceramic slurry was printed using a DLP 3D printer (Jiaxing Selamga Technology Co., Ltd., China) equipped with a 385 nm ultraviolet light source to obtain green bodies. Three types of samples were fabricated: (i) Bar-shaped samples (45 mm × 5 mm × 4 mm) for mechanical testing and microstructural observation, (ii) accuracy-test blocks (15 mm × 10 mm × 3 mm) containing circular holes of 2.0, 1.6, 1.2, 1.0, 0.8, 0.6, 0.4, and 0.2 mm in diameter (Fig. 3), and (iii) circular samples (15 mm in diameter and 1.5 mm in height) were used for antibacterial and translucency evaluations.

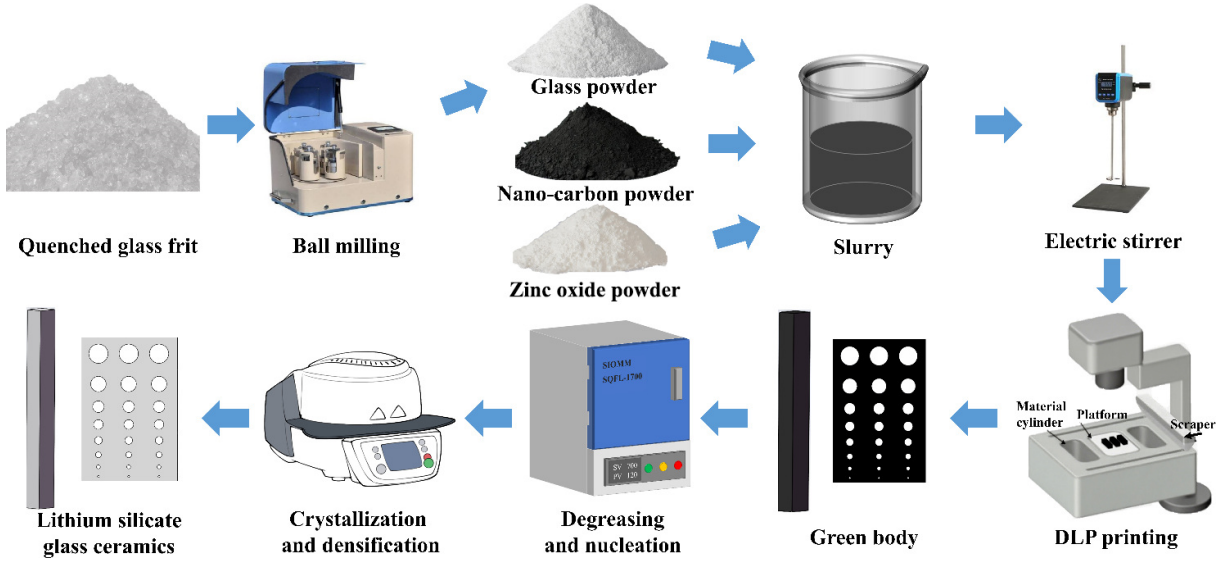

Fig. 1 Preparation process of glass-ceramics.

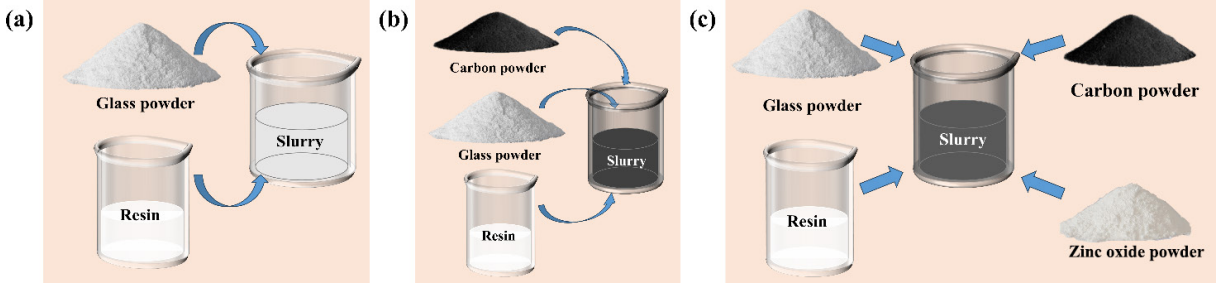

Fig. 2 Schematic diagram of preparation of slurry for each group: (a) LD group, (b) LDC_x group, and (c) LDC_xZn_y group.

To identify the optimal contents of C and ZnO, single-layer exposure tests were first conducted on the hole-containing samples. After printing a single layer, the dimensional accuracy and curing thickness were evaluated to screen for favorable compositions. Dimensional accuracy was characterized by measuring the dimensional deviation of the printed holes from their designed diameters, while curing depth was determined using a micrometer. Initially, single-layer LD hole samples were fabricated under varying light intensities to establish a baseline. Based on optical simulation results, samples with C contents of 0, 0.2, 0.4, and 0.6 wt% and ZnO contents of 0, 2.5, and 4.5 wt% were subsequently prepared for single-layer curing tests. The choice of ZnO concentrations was informed by optical simulation results as well as by literature studies on their satisfactory antibacterial performance [24,34,35].

The printing process was conducted with a scanning speed of 3000 mm/s and a layer thickness of 40 μm. To achieve a consistent curing depth of approximately 130 μm (Table 1), the laser power was adjusted accordingly. This necessity arose from the high extinction coefficient of C, which led to significant light absorption and thus required higher ultraviolet light intensity to achieve the target curing depth [15,36]. Dimensional accuracy was evaluated by measuring holes across three replicate samples in each group and calculating the deviation from the designed values.

To identify key thermal parameters—including the debinding temperature, the crystallization temperatures of lithium metasilicate (Li_2SiO_3) and lithium disilicate ($Li_2Si_2O_5$), and the glass melting temperature—for establishing the optimal heating profile, the green bodies of LD, $LDC_{0.4}Zn_{2.5}$, and $LDC_{0.4}Zn_{4.5}$ were analyzed by a synchronous thermal analyzer (METTLER TOLEDO-TGA/DSC 3 + , Switzerland). This analysis provided simultaneous thermogravimetric (TG) and differential scanning calorimetry (DSC) data in air at a heating rate of 10 °C/min. Subsequently, the apparent porosity of the fracture surfaces of the sintered samples was assessed using ImageJ software. Informed by studies that multistage heat treatment could mitigate sintering defects in additively manufactured lithium disilicate [37,38], a two-step thermal schedule was adopted. The first step involved debinding in a muffle furnace (KSL-1200X, Hefei Kejing, China) under an air atmosphere. The second step was carried out in a vacuum ceramic furnace (P300, Ivoclar Vivadent, Liechtenstein), where the samples were sintered under vacuum to promote nucleation and crystallization, followed by a final heating stage to achieve full densification via viscous flow. The vacuum environment was essential for two reasons: First, to prevent air entrapment in surface micropores remaining after debinding, thereby facilitating porosity reduction [5]; second, to protect highly reactive lithium ions from oxidation at elevated temperatures.

2.2.4 *Characterization*

Rheological behavior, light curing, and sedimentation behavior of slurry

Each group of suspensions was prepared by uniform mixing under identical conditions. Their viscosity was first characterized using a viscometer (NDJ-9S, Shanghai LiChen Co., China). Following this, the suspensions were transferred to glass vials for sedimentation monitoring, with observations recorded at days 1, 5, and 7. The sedimentation rate S was determined by the initial slurry height (H) and the height of the clarified sedimentation layer (H_1), as given by Eq. (1) [39].

$$S = \frac{H_1}{H} \tag{1}$$

To study the photopolymerization kinetics, the slurries were irradiated with different light powers. The curing depth (C_d) after each exposure was measured using a micrometer, and the exposure energy (E) was calculated as the product of exposure time and power. Jacob's working curve equation was then applied to establish the logarithmic relationship between C_d and E, as given by Eq. (2) [39].

$$C_d = D_p \ln\left(\frac{E}{E_s}\right) = D_p(\ln E - \ln E_s) \tag{2}$$

where D_p denotes the penetration depth (or sensitivity coefficient), and E_s represents the critical exposure energy in the curing depth direction.

Deformation, shrinkage, and accuracy

The dimensional accuracy of the 3D printing process was

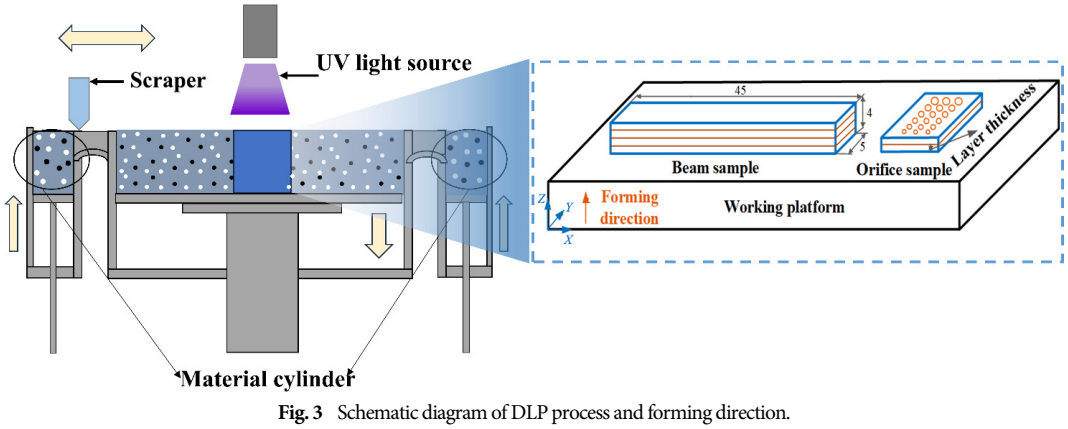

Fig. 3 Schematic diagram of DLP process and forming direction.

Table 1 Printing parameters corresponding to each group of slurries

Group	C powder content (wt%)	ZnO content (wt%)	Scanning speed (mm/s)	Power (mW/cm²)	Exposure time (s)	Layer thickness (μm)
LD	0	0	3000	20	3	40
$LDC_{0.4}$	0.4	0	3000	90	3	40
$LDC_{0.4}Zn_{2.5}$	0.4	2.5	3000	90	3	40
$LDC_{0.4}Zn_{4.5}$	0.4	4.5	3000	90	3	40

evaluated by measuring the holes in the green body samples using an image measuring instrument (KYVMS-3020, Dongguan Keruy Optical Instrument Co., Ltd., China). The measured dimensions of the holes were compared with their original design values to quantify the printing fidelity. Meanwhile, the linear shrinkage of the bar samples after sintering was determined by measuring their dimensions in both the green and sintered states using a vernier caliper. The linear shrinkage was then calculated from these measurements according to Eq. (3):

$$\delta = \frac{l_0 - l_1}{l_0} \times 100\% \tag{3}$$

where δ represents the linear shrinkage rate, l_0 denotes the dimension of the sample after printing, and l_1 indicates the dimension after sintering [22].

Microstructure

The surface morphology and crystalline phase of the starting materials (including glass, C, and ZnO powders) and the polishing sintered samples were characterized using a field emission scanning electron microscope (FE-SEM; JEOL JSM-7610F, Japan) and an X-ray diffractometer (XRD; Rigaku SmartlabSE, Japan). XRD analysis was performed over a 2θ range of 10°–60° at a scanning rate of 10°/min with a step size of 0.02° to identify the crystalline phases. Additionally, the porosity of the samples was quantified using ImageJ software and calculated as the ratio of the total pore area to the total analyzed area. The transmittance of 1.0 mm-thick circular samples was measured using a spectrophotometer (UH4150, HITACHI, China) over the wavelength range of 380–780 nm.

Mechanical performances

The mechanical properties, including flexural strength, elastic modulus, Vickers hardness, and fracture toughness, were evaluated for various sintered sample groups, and fatigue testing was performed on the $LDC_{0.4}Zn_{2.5}$ sample. The flexural strength and elastic modulus were determined via a three-point bending test performed on a universal electronic testing machine (MTS CMT3004, China) at a loading speed of 0.5 mm/min and a span of 30 mm. The flexural strength and elastic modulus (E_1) were calculated according to Eqs. (4) [18] and (5) [40], respectively:

$$\sigma_f = \frac{3FL}{2bh^2} \tag{4}$$

$$E_1 = \frac{FL^3}{4bh^3d} \tag{5}$$

where F is the applied load; L represents the span; b denotes the width of the sample; h is the height of the sample; d indicates the displacement produced under the load (F).

The samples were ground sequentially with 400–2000 mesh silicon carbide sandpapers and finally polished with diamond paste. Vickers hardness was determined under a 1000 N load held for 15 s (Wilson 402MVD, USA), following ISO 14705. Fracture toughness was assessed on bar-shaped samples via the indentation method [41], whereby crack lengths originating from the Vickers indent were measured and used to calculate toughness values with Eq. (6):

$$K_{IC} = 0.016 \left(\frac{E_1}{H_v}\right)^{\frac{1}{2}} \frac{P}{C^{\frac{3}{2}}} \tag{6}$$

where H_v denotes the Vickers hardness, and c represents the half-length of the indentation-induced crack.

The fatigue test adopted the step stress method. The fatigue equipment was an electronic universal tension/torque mechanics test system (EUM-10k, CARE Measurement & Control Technology (Tianjin) Co., Ltd., China). The frequency was selected as 2 Hz. According to the ASTM standard, at the beginning of the test, 10,000 cycles were carried out with a load of 130 N. Subsequently, the load was gradually increased by 21 N every 10,000 cycles until the sample broke. At the end of each test, the fatigue failure load (FFL) and cycles for failure (CFF) data were recorded.

Antibacterial performance test

Streptococcus mutans (*S. mutans*, Gram-positive) and *Escherichia coli* (*E. coli*, Gram-negative) were employed as representative cocci to evaluate the antibacterial efficacy of the material. 6 mL of each bacterial suspension was added to 54 mL of sterile Luria–Bertani (LB) broth and brain heart infusion (BHI) broth prepared in the laboratory and incubated for 24 h at 100 r/min. The bacterial suspension was then diluted to 1×10^6 CFU/mL (CFU = colony forming unit) and held ready. Antibacterial testing was performed with disk-shaped samples ($d \times h$ = 15 mm × 5 mm), and the antimicrobial rate was calculated by the plate-count method. After thorough rinsing with ethanol, each sample was exposed to ultraviolet (UV) light for 30 min for sterilization, transferred into a 24-well cell culture plate, and kept ready for use. 500 mL of the bacterial suspension was placed on each sample and incubated together in an incubator. After 24 h, 100 μL was withdrawn from every well and serially diluted to 10^3 CFU/mL, and 100 μL of the dilution was spread onto agar plates. *E. coli* growth was examined and quantified following 12 h of incubation, whereas *S. mutans* growth was assessed and enumerated after 48 h of incubation. To evaluate the long-term antibacterial activity, after the initial solution was removed, 200 μL of the same bacterial suspension was added to each well for continued co-culture. After 48 h, 100 μL was taken for serial dilution and spread onto agar plates, and this process was repeated. Long-term antibacterial activity was assessed based on the material's inhibitory efficacy on days 1, 3, and 5.

Statistical analysis

Mechanical properties and antibacterial experiments were conducted with replicate measurements: flexural strength, Vickers hardness, and fatigue tests were performed with 10 replicates, while fracture toughness and elastic modulus tests were performed with 5 replicates. Bacterial assays were conducted in three independent experiments. All data were expressed as the mean ± standard deviation. Statistical analysis was performed using one-way analysis of variance (ANOVA), with Tukey's post hoc test used for multiple comparisons between groups. A p-value < 0.05 was considered statistically significant.

3 Results and discussion

3.1 Characterization of glass powder and slurry

The morphology, particle size distribution, and phase composition of the raw powders (glass, C, and ZnO) were characterized, as shown in Fig. 4. The morphology of the particles was characterized using SEM (Figs. 4(a)–4(c)). The particle size distribution was then determined through statistical analysis using ImageJ software (Figs. 4(d)–4(f)), with at least 5 fields of view and 500 particles recorded for each sample [38]. The ceramic-milled glass powder consisted of irregular, sharp-edged particles with a broad size distribution (Figs. 4(a) and 4(d)). Its relative frequency maximum at 4–7 μm and median size of 4.8 μm indicated that most particles fell within this range. C powder appeared as fine, spherical particles with a mean diameter of 45.1 nm (Figs. 4(b) and 4(e)), while ZnO comprised irregular polygons with a median size of 5.6 μm (Figs. 4(c) and 4(f)). These observations aligned with the geometries and dimensions used in the optical

simulations. XRD analysis (Fig. 4(g)) confirmed the amorphous nature of the glass powder. The C powder showed a broad hump centered at approximately 22.78°, characteristic of amorphous C. The XRD pattern of ZnO matched the standard hexagonal phase (PDF#36-1451) without detectable impurities.

The rheological properties of the suspensions, critical for DLP printing [39], are presented in Fig. 4(h). The $LDC_{0.4}$ slurry exhibited higher viscosity than LD, possibly due to the high specific surface area of nano-C, which enhanced interparticle forces and promoted network formation [42]. With the addition of 2.5 wt% ZnO, the viscosity decreased as the larger particles increased the interparticle spacing. However, a further increase to 4.5 wt% ZnO caused slight agglomeration, increasing the solid surface area and resulting in a minor viscosity rebound. Notably, the viscosity of all slurries remained within the printable range.

An ideal slurry for 3D printing should simultaneously exhibit high solid loading and low viscosity [22]. However, these two properties are often contradictory: High solid loading typically increases viscosity due to greater particle interactions, while low solid loading, although reducing viscosity, compromises the mechanical properties of the sintered parts [22]. In this study, our composite design successfully decoupled this trade-off. By maintaining a constant solid loading, the strategy achieved both high solid content and reduced viscosity, resulting in favorable fluidity that enhanced printing accuracy. Furthermore, Fig. 4(i) shows that the initial slurry volume was set at 10 mL. The LD group exhibited a decrease of approximately 0.5 mL by the seventh day, resulting in a sedimentation rate of approximately 5% over this period. In contrast, no significant sedimentation was noted for any of the other slurries during the same timeframe (Fig. 4(i)). This improved stability was attributed to the high specific surface area of C and ZnO particles, which increased interfacial contact and strengthened surface interactions, thereby inhibiting sedimentation and enhancing the overall stability of the photopolymerizable paste.

3.2 Light scattering in composite materials

The optical behaviors of the resin, LD, $LDC_{0.4}$, and $LDC_{0.4}Zn_{2.5}$ suspensions are represented by models in Figs. 5(a)–5(d). The light–matter interaction is governed by core parameters such as the complex refractive index, $m = n + ik$ (where n is the refractive index and k is the extinction coefficient), which defines a material's fundamental optical properties [15]. Light scattering occurs when light propagates through an inhomogeneous medium and encounters regions with differing refractive indices, leading to random changes in propagation direction and energy dispersion. As Fig. 5(a) shows, a single homogeneous material exhibited no scattering, with a curing depth and width of approximately 31 and 5 μm, respectively. However, introducing glass powder into the resin created a highly inhomogeneous system. The inherent transparency of the glass, coupled with the refractive index mismatch with the resin, resulted in severe scattering and

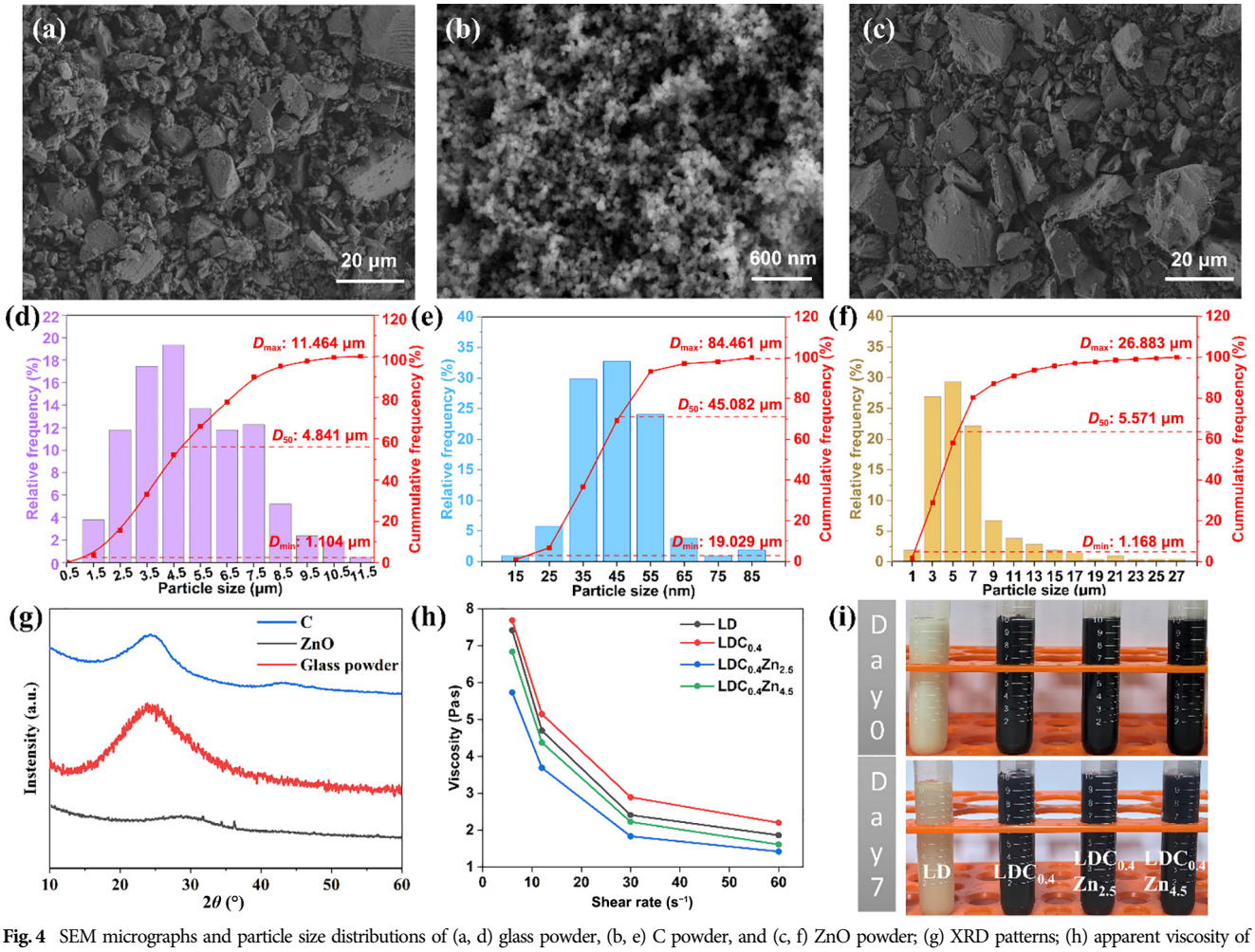

Fig. 4 SEM micrographs and particle size distributions of (a, d) glass powder, (b, e) C powder, and (c, f) ZnO powder; (g) XRD patterns; (h) apparent viscosity of as-prepared slurry at shear rates of 6, 12, 30, and 60 s^{-1}; (i) sedimentation behavior of slurry at 35 °C, where D_{max}, D_{50}, and D_{min} represent the maximum, average and minimum particle sizes, respectively.

excessively large curing depth and width, reaching 28 and 31 μm, respectively, as depicted in Fig. 5(b).

The addition of C powder with a high extinction coefficient significantly reduced scattering through strong absorption of scattered light, where both curing depth and width were reduced to approximately 10 and 8 μm, respectively (Fig. 5(c)). This excessive absorption could lead to undercuring and weak interlayer bonding. In contrast, the codoping of C and ZnO (Fig. 5(d)) yielded a more balanced outcome, achieving a curing depth of 16 μm and a width of 9 μm. While C confined the light, ZnO, with its lower extinction coefficient, increased the refractive index, moderately expanding the refraction, reflection, and diffraction of light. This mitigated the over-absorption by C, thereby increasing the curing depth without a substantial increase in width. The trend of the simulation results demonstrated that this synergistic effect enhanced both the printing accuracy and the curing quality, confirming the feasibility of optimizing the slurry's optical parameters through composite material design.

3.3 3D printing accuracy

The experimental results for printing accuracy, summarized in Fig. 6, confirmed the trends predicted by finite element simulations. The analysis of hole radius errors (Figs. 6(a)–6(c)) revealed that accuracy was primarily governed by C content. Increasing the C content from 0 to 0.4 wt% progressively reduced the light scattering and curing depth (Fig. 6(d)), thereby minimizing the radial error (Fig. 6(a)). This phenomenon arose from the high extinction coefficient of C. Optical simulations demonstrated that C absorbed substantial light energy, diminishing light scattering, light transmittance, and curing depth. Higher C contents enhanced light absorption capacity, impeding light transmission to deeper regions and consequently reducing irradiation depth. As a result, the curing depth decreased monotonically with increasing C content. When the C content exceeded 0.4 wt%, an increase in C content significantly reduced the optical penetration of the slurry, leading to a notable decline in curing depth. To compensate, a higher light power was required to achieve an adequate curing depth (Fig. 6(d)). However, increasing the light intensity also elevated the curing width, which in turn limited further improvements in fabrication accuracy.

While C optimized in-plane (*XY*) resolution, ZnO was crucial for through-thickness (*Z*-axis) properties. Although ZnO addition had little impact on the planar dimensional error of the $LDC_{0.4}$ baseline (Fig. 6(b)), it systematically increased the curing depth (Fig. 6(e)). This counteracted the excessive light absorption of C, rectifying the undercuring issue sketched in Fig. 6(f). By ensuring adequate penetration for robust interlayer bonding without sacrificing planar accuracy, the $LDC_{0.4}Zn_{2.5}$ composite achieved an optimal balance, leading to improved mechanical performance and validating our composite design strategy.

Based on the finite element analysis and experimental validation, four slurry compositions—LD, $LDC_{0.4}$, $LDC_{0.4}Zn_{2.5}$, and $LDC_{0.4}Zn_{4.5}$—were selected for further testing. As shown in Fig. 6(g), the DLP-printed green bodies and the corresponding sintered parts for these groups. The LD group could only form a minimum hole size of 1.6 mm, whereas the $LDC_{0.4}$, $LDC_{0.4}Zn_{2.5}$, and $LDC_{0.4}Zn_{4.5}$ groups all achieved a significantly finer minimum feature size of 0.4 mm (Fig. 6(g)). This improvement was attributed to the low extinction coefficients of the resin and parent glass, which allowed light to penetrate deeply. During layer-by-layer exposure, this stray light could overcure previously solidified layers, leading to overall shrinkage, deformation, and the clogging of fine features. The incorporation of C powder introduced a high extinction coefficient, effectively confining the light and thus enabling the superior accuracy observed in the C-containing groups.

The $LDC_{0.4}Zn_{4.5}$ sample yielded the highest precision, with radius errors as low as 0.013 mm for the 2 mm hole and 0.0143 mm for the 1.6 mm hole (Fig. 6(c)), showing excellent agreement with the finite element simulation results. Furthermore, as evident from

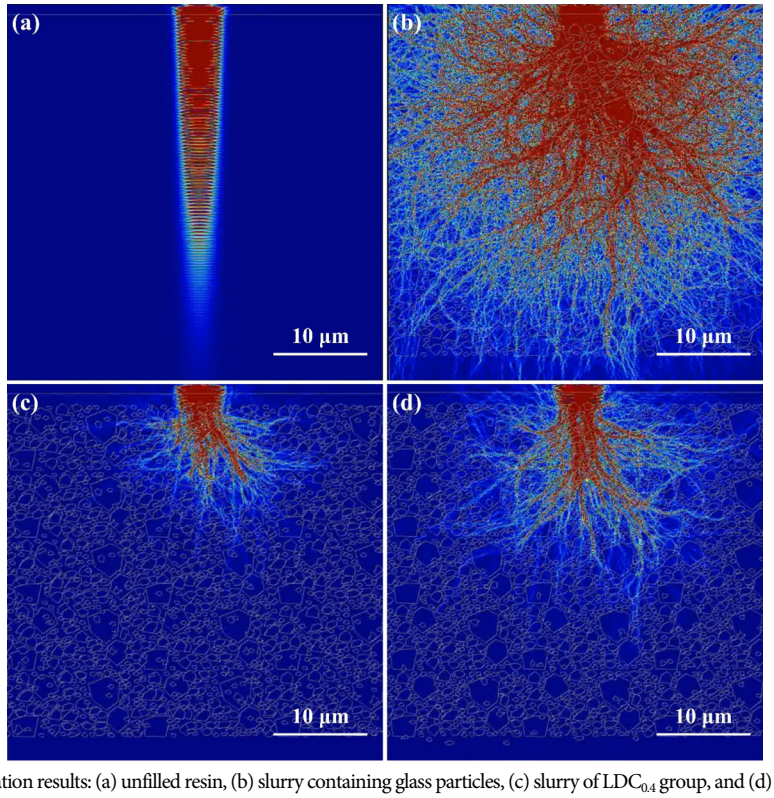

Fig. 5 Light scattering simulation results: (a) unfilled resin, (b) slurry containing glass particles, (c) slurry of $LDC_{0.4}$ group, and (d) slurry of $LDC_{0.4}ZnO_{2.5}$ group.

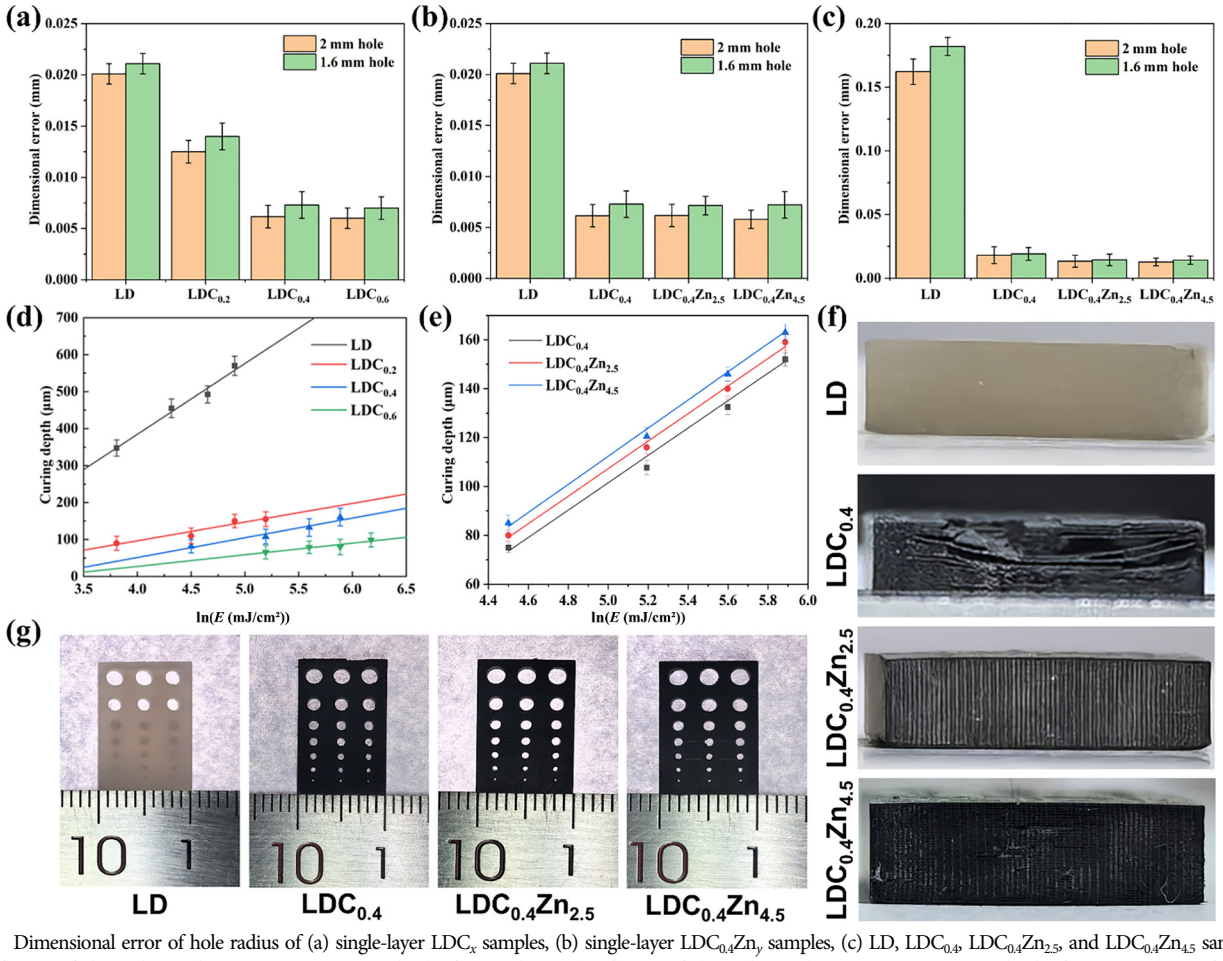

Fig. 6 Dimensional error of hole radius of (a) single-layer LDC_x samples, (b) single-layer $LDC_{0.4}Zn_y$ samples, (c) LD, $LDC_{0.4}$, $LDC_{0.4}Zn_{2.5}$, and $LDC_{0.4}Zn_{4.5}$ samples, (d) influence of ultraviolet irradiation energy on curing depth of LDC_x slurry, (e) influence of ultraviolet irradiation energy on curing depth of LDC_xZn_y slurry, (f, g) 3D printed and sintered pore samples.

the photographs of the printed green bodies in Fig. 6(f), the sample containing only C exhibited interlayer cracks, whereas the sample codoped with both C and ZnO demonstrated significantly improved print quality. These results confirmed that the simultaneous incorporation of C and ZnO substantially enhanced printing precision, curing depth, and overall print quality.

3.4 Debinding and sintering strategy

Following printing, the green body underwent debinding to remove organic components and C, followed by sintering to achieve crystallization. The thermal schedules for both debinding and sintering were designed based on the TG–differential thermogravimetry (DTG) and DSC results, respectively [37,38]. The TG–DTG analysis (Fig. 7(a)) indicated a total mass loss of 36.63% below 500 °C, with the loss rate becoming negligible above 550 °C. Accordingly, a debinding program was established with holding stages at 350, 450, and 550 °C (2 h each) and a heating rate of 3 °C/min to ensure thorough removal while minimizing defects (Fig. 7(c)).

Based on DSC analysis, sintering temperature profiles were designed for three groups: LD, $LDC_{0.4}Zn_{2.5}$, and $LDC_{0.4}Zn_{4.5}$ (Figs. 7(d)–7(f)). The DSC results (Fig. 7(b)) exhibited an endothermic peak at 900–940 °C, corresponding to the glass melting temperature (T_m) [43,44]. Vacuum sintering at T_m enabled densification of lithium silicate glass-ceramics through viscous flow without deformation [38]; therefore, 900–940 °C was selected as the sintering temperature. To optimize the process parameters, three densification temperatures were tested for each composition: 905, 925, and 945 °C for the LD and $LDC_{0.4}$ groups (Fig. 7(d)); 900, 920, and 940 °C for the $LDC_{0.4}Zn_{2.5}$ group (Fig. 7(e)); and 900, 910, and 920 °C for the $LDC_{0.4}Zn_{4.5}$ group (Fig. 7(f)). Since the C powder was entirely removed during the debinding stage, the LD and $LDC_{0.4}$ groups shared an identical sintering curve. The optimal sintering temperature for each composition was subsequently determined by evaluating the corresponding microstructural properties.

3.5 Microstructure

To evaluate the influence of heat treatment temperature on densification, the fracture morphologies of samples sintered at different temperatures were analyzed. As shown in Fig. 8, while the specific optimal temperature differed, all compositions showed a common densification trend. For the LD group (Fig. 8(a)), sintering at 905 °C yielded a structure with fine pores. Increasing the temperature to 925 °C reduced the glass phase viscosity, facilitating pore filling and shrinkage via viscous flow in accordance with the Frenkel model [45]. However, further heating to 945 °C was detrimental: Rapid grain boundary migration traps pores, while Ostwald ripening led to pore coarsening [46]. The incorporation of ZnO lowers the temperature required for densification. It acted as a flux, reducing glass phase viscosity to improve particle wetting and accelerate diffusion, which in turn enhanced pore closure. Therefore, considering both macroscopic form and microstructure, the optimal sintering conditions were established at 925 °C for LD and $LDC_{0.4}$, 920 °C for $LDC_{0.4}Zn_{2.5}$, and 910 °C for $LDC_{0.4}Zn_{4.5}$.

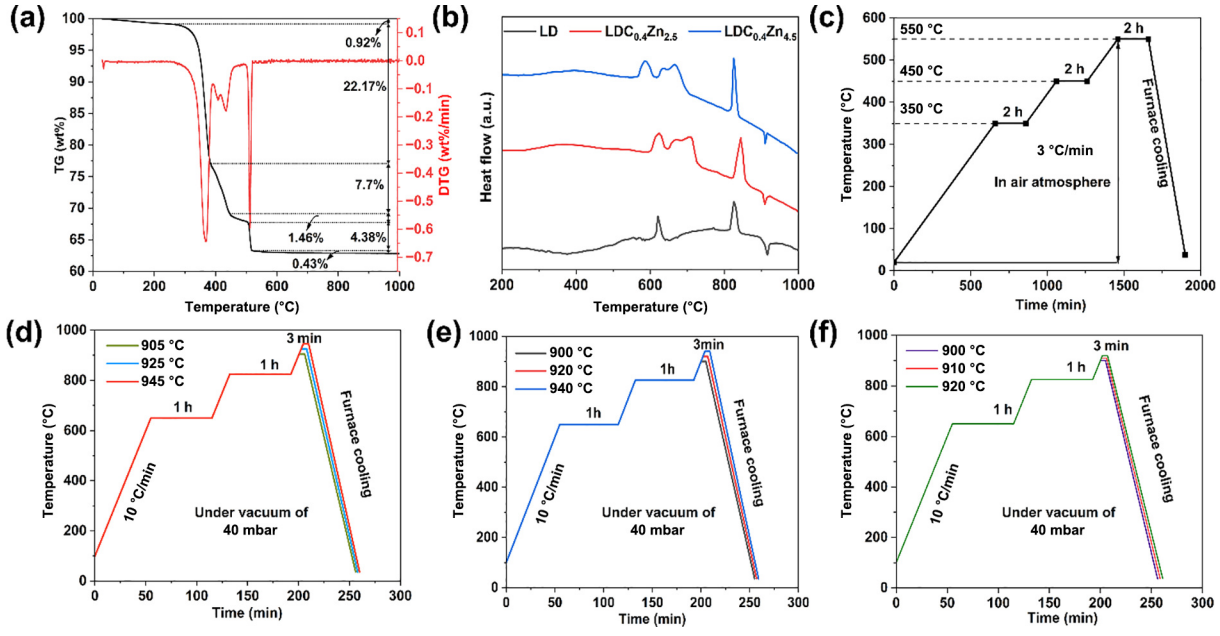

Fig. 7 (a) TG–DTG curves of green body, (b) DSC curves of LD, $LDC_{0.4}Zn_{2.5}$, and $LDC_{0.4}Zn_{4.5}$, (c) debinding curve, (d–f) sintering curves of LD, $LDC_{0.4}Zn_{2.5}$, and $LDC_{0.4}Zn_{4.5}$.

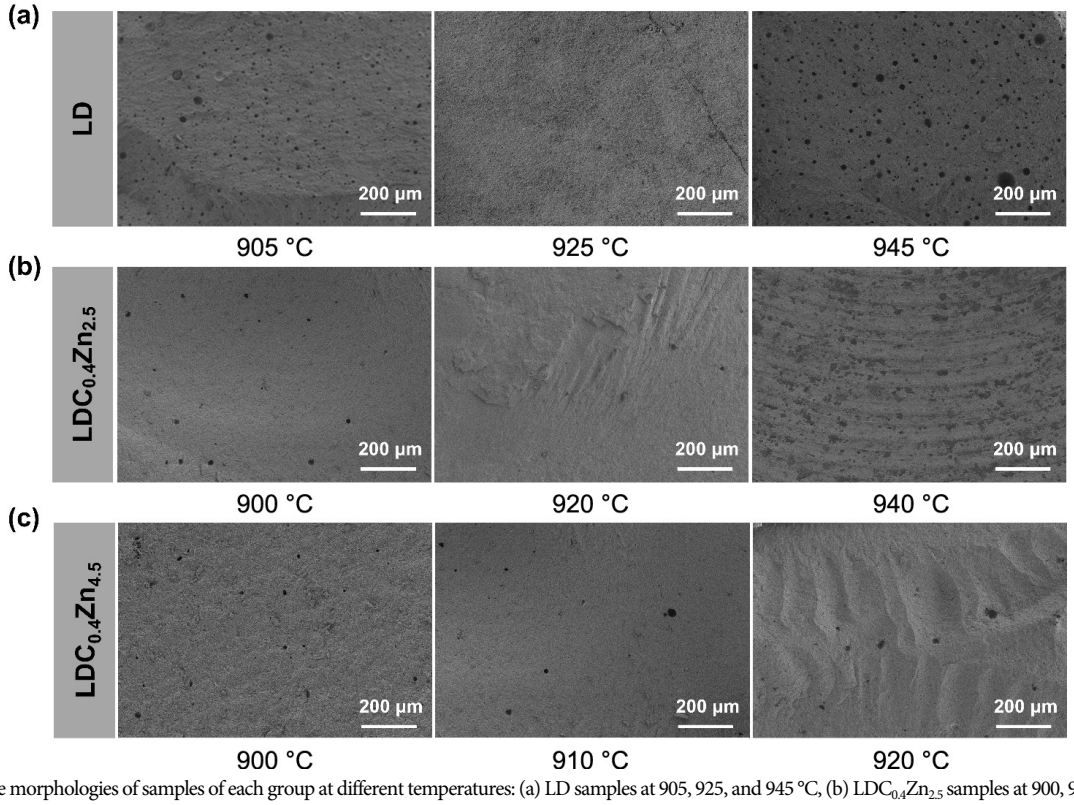

Fig. 8 Fracture morphologies of samples of each group at different temperatures: (a) LD samples at 905, 925, and 945 °C, (b) $LDC_{0.4}Zn_{2.5}$ samples at 900, 920, and 940 °C, and (c) $LDC_{0.4}Zn_{4.5}$ samples at 900, 910, and 920 °C.

3.6 Appearance and XRD of glass-ceramics

Figures 9(a)–9(d) present the green bodies, debinded samples, and sintered samples (from top to bottom, respectively) for each group. The green bodies containing C appear black, whereas all debinded samples exhibited a consistent color, confirming the complete removal of C during the debinding process. When sintered at their respective optimal temperatures, all samples maintained structural integrity without deformation.

As shown in Fig. 9(e), the linear shrinkage rates of the four groups were nearly identical along the length, width, and height directions. However, each group exhibited the greatest shrinkage along the build (height) direction, a common phenomenon in vat-photopolymerized ceramics that was primarily attributed to gravitational particle settling during printing.

The XRD patterns in Fig. 9(f) reveal the phase evolution of the four groups. In the $LDC_{0.4}$ sample, the gases released during C removal likely hindered intergranular contact, resulting in an amorphous hump and reduced crystallinity. In contrast, the

$LDC_{0.4}Zn_{2.5}$ and $LDC_{0.4}Zn_{4.5}$ samples showed sharper and more intense $Li_2Si_2O_5$ diffraction peaks, indicating enhanced crystallinity. This improvement could be ascribed to the formation of chemically stable and biocompatible Zn_2SiO_4 [47], which also helped suppress abnormal grain growth, thereby improving microstructural stability. Moreover, the absence of peak shifts in any of the compositions confirmed that the incorporation of C and ZnO did not significantly distort the crystal lattice. The translucency characteristics are demonstrated in Figs. 9(g)–9(j). $LDC_{0.4}$ exhibited no significant change compared with LD, as C oxidized and decomposed during debinding. However, ZnO incorporation led to a slight decrease in translucency, which became more evident with increasing ZnO content. Nevertheless, all four glass-ceramics clearly revealed the underlying black-and-white pattern. Quantitative transmittance results (Fig. 9(k)) showed values exceeding 50% for all samples, confirming their good translucency. Consequently, the aesthetic quality of lithium disilicate glass-ceramics, a critical property for dental restorations, remained uncompromised by the composite design.

3.7 Mechanical performances

The load–displacement curves in Fig. 10(a) demonstrated typical brittle fracture behavior for all samples. Figures 10(c) and 10(d) present the flexural strength, elastic modulus, Vickers hardness, and fracture toughness of the sintered glass-ceramics. The mechanical properties across the four groups followed a consistent trend. Specifically, $LDC_{0.4}$ exhibited a reduction in the mechanical performances compared with LD samples. This degradation was attributed to two primary factors. First, as predicted by the optical simulation, the high light absorption of C powder reduced the curing depth and width, which weakened interlayer adhesion during printing and could lead to internal pores or insufficiently cured regions. Second, the volatilization of C during debinding generated additional porosity (Fig. 10(b)), thereby increasing the overall porosity and reducing the structural density of the sintered body.

The $LDC_{0.4}Zn_{2.5}$ and $LDC_{0.4}Zn_{4.5}$ composites exhibited superior mechanical properties and reduced porosity compared with $LDC_{0.4}$, with performance levels matching or surpassing those of the LD. Among them, the $LDC_{0.4}Zn_{2.5}$ composition was identified as optimal, demonstrating a marked enhancement in key properties over LD, including a flexural strength of 297.28±10 MPa, an elastic modulus of 149±2.5 GPa, a Vickers hardness of 6.12±0.12 GPa, and a fracture toughness of 3.74±0.05 $MPa{\cdot}m^{1/2}$. Notably, the performance of $LDC_{0.4}Zn_{2.5}$ exceeded that reported in several previous studies on DLP-printed lithium silicates [13,37,38]. This trend in mechanical properties arose from the interplay of several mechanisms. Positively, ZnO acted as a sintering aid, facilitating liquid-phase sintering that enhanced particle rearrangement and densification, thereby healing the pores and cracks initially introduced by C. Additionally, ZnO could adsorb onto C particles, mitigating their agglomeration and indirectly improving interlayer bonding. However, at higher concentrations (e.g., 4.5 wt%), ZnO nanoparticles themselves tended to agglomerate, creating stress concentrators that counteracted the beneficial effects. Furthermore, the thermal expansion mismatch between ZnO (~4.75×10^{-6} K^{-1}) and the matrix ($Li_2Si_2O_5$ crystal: 10.18×10^{-6}–10.8×10^{-6} K^{-1}; glass matrix: 12.28×10^{-6}–12.8×10^{-6} K^{-1}) introduced complex interfacial stresses [37,48]. A moderate mismatch can induce tangential compressive

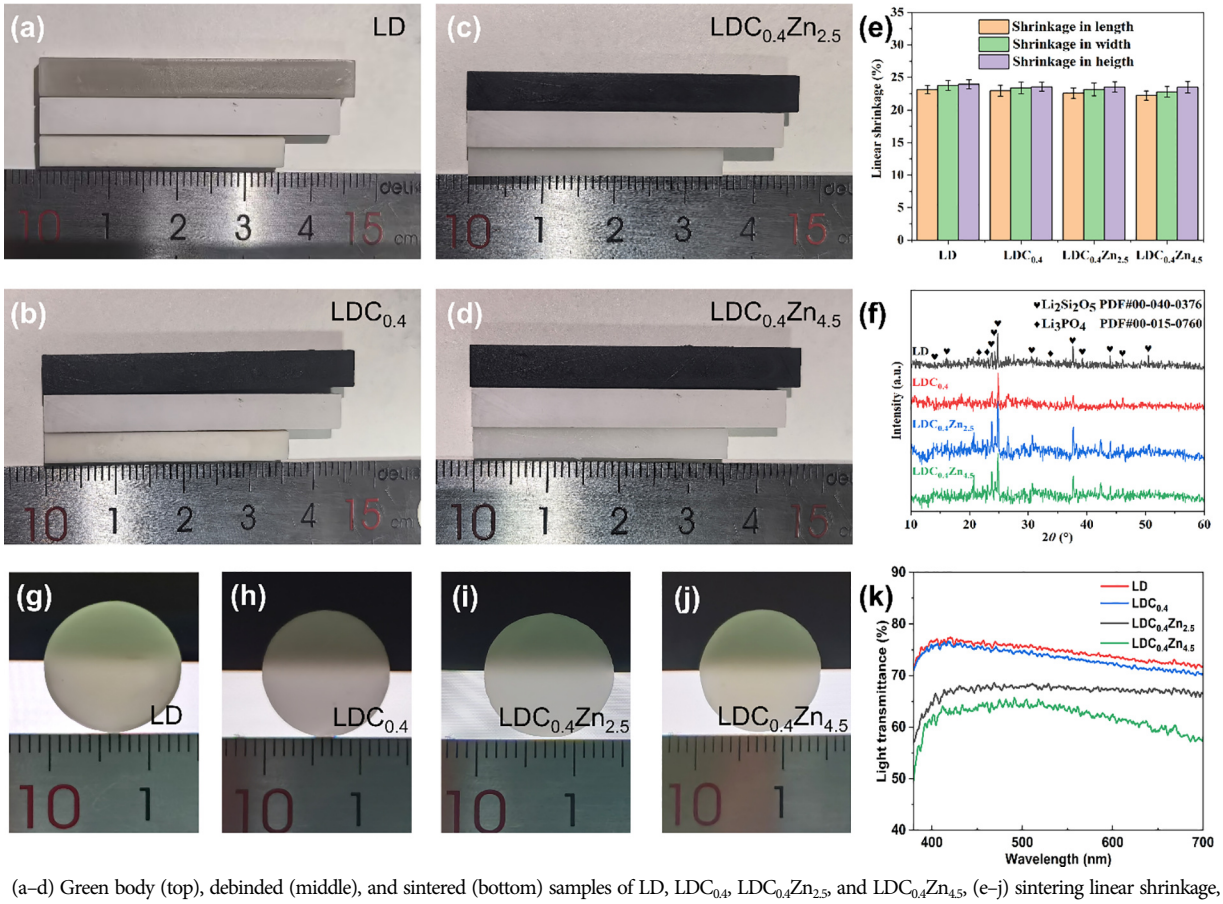

Fig. 9 (a–d) Green body (top), debinded (middle), and sintered (bottom) samples of LD, $LDC_{0.4}$, $LDC_{0.4}Zn_{2.5}$, and $LDC_{0.4}Zn_{4.5}$, (e–j) sintering linear shrinkage, XRD patterns, and photographs of LD, $LDC_{0.4}$, $LDC_{0.4}Zn_{2.5}$, and $LDC_{0.4}Zn_{4.5}$, (k) light transmittance curve.

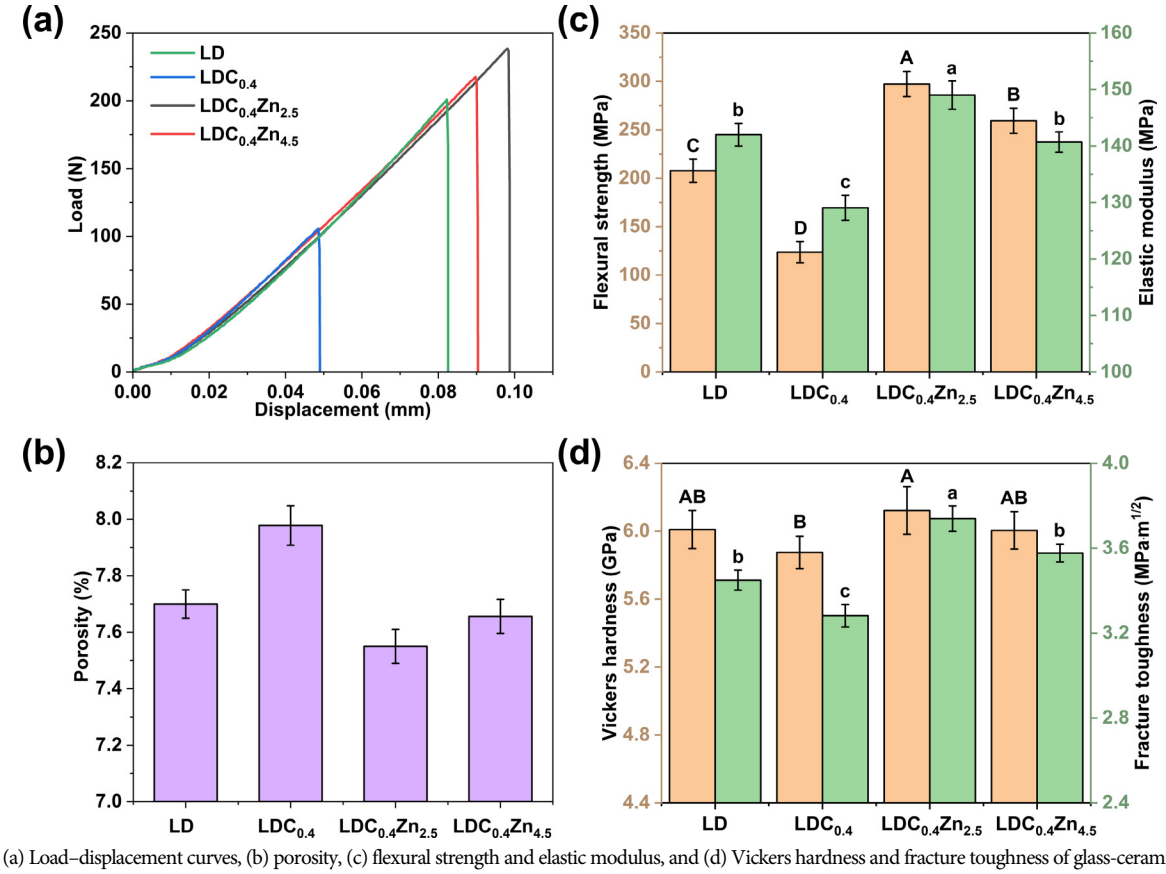

Fig. 10 (a) Load–displacement curves, (b) porosity, (c) flexural strength and elastic modulus, and (d) Vickers hardness and fracture toughness of glass-ceramics. Values with the same uppercase or lowercase letters in each figure are not significantly different at $\alpha = 0.05$ (α represents the significance level).

Table 2 Comparative analysis of mechanical properties of lithium silicate glass-ceramics

Author	Forming technology	Flexural strength (MPa)	Vickers hardness (GPa)	Fracture toughness (MPa·m$^{1/2}$)
Baumgartner *et al.* [5]	DLP	400	6.75	2.96
Marsico *et al.* [13]	DLP	290±60	5.5±0.3	2.07±0.22
Ma *et al.* [37]	DLP	275±40	5.2±0.1	3.4±0.2
Zhou *et al.* [38]	DLP	284.5±37.0	5.2±0.3	2.3±0.1
Alves *et al.* [50]	LCD	281±37	5.3±0.2	—
This work	DLP	297.28±10	6.122±0.12	3.74±0.052

stresses around crystals, promoting crack deflection and enhancing toughness [49]. However, an excessive mismatch, as in $LDC_{0.4}Zn_{4.5}$, led to severe stress concentration at the interface, potentially causing microcracking or delamination and thus degrading the overall mechanical performance [37]. Consequently, the $LDC_{0.4}Zn_{2.5}$ composition achieved an optimal balance, yielding the most favorable set of properties. A comparison with existing 3D-printed lithium silicate glass-ceramics (Table 2) indicated that optimization of slurry composition, debinding process, and sintering conditions could effectively tailor printing accuracy, pore structure, and mechanical properties. Therefore, this study provided a feasible technical route for DLP fabrication of high-performance LD ceramics.

The load–number of cycle curve depicted in Fig. 11 demonstrated that the sample exhibited no fracture under the first five stepwise load levels (130, 151, 172, 193, and 214 N, each applied for 10,000 cycles at a stress ratio $R = 0.1$), with instantaneous failure occurring only during the initial loading stage of the sixth step (214–235 N). As illustrated in Table 3, only sample 4 fractured at the terminus of the fifth step (193–214 N), while all other samples underwent abrupt fracture during the loading phase of the sixth step, manifesting characteristic failure features of brittle ceramic materials. The average fatigue fracture load for the 3D-printed lithium disilicate glass-ceramic was measured to be 225.82±22.5 N in this study.

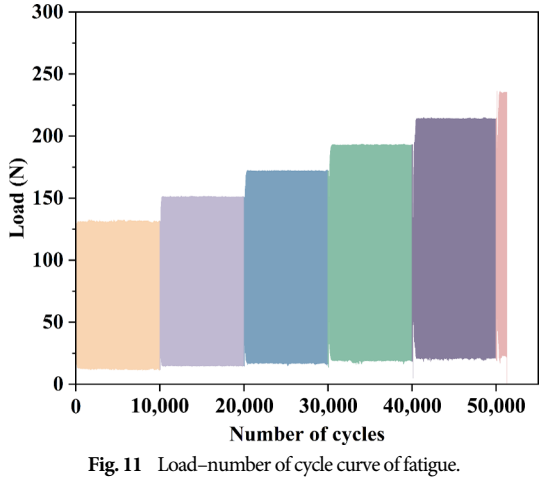

Fig. 11 Load–number of cycle curve of fatigue.

清華大學出版社 Tsinghua University Press | SciOpen

Such brittle fracture behavior, in conjunction with the material properties of lithium disilicate glass-ceramic, suggested that its fatigue failure likely followed a subcritical crack growth mechanism, which was fundamentally consistent with the environmentally assisted fracture behavior of ceramics described in standards such as ASTM C1368. Compared with the fatigue fracture loads of conventionally pressed lithium disilicate glass-ceramics (313–435 N) [51], the fracture loads of the material investigated herein were moderately lower, primarily attributed to insufficient microstructural densification resulting from the 3D printing process. The fatigue experiments substantiated that the lithium disilicate glass-ceramic fabricated via the composite powder design approach possessed certain fatigue resistance stability, although it required further improvement relative to conventional fabrication processes.

3.8 Antibacterial performance

S. mutans and *E. coli*, representative Gram-stained cocci, were used to verify the antibacterial efficacy of the material. As shown in Fig. 12(a), the viable counts of both species dropped markedly after ZnO doping, indicating that ZnO significantly enhanced the antibacterial activity. The quantitative antibacterial results are presented in Figs. 12(b)–12(d). On the first day, the ZnO-containing material inhibited both bacterial strains by over 90%, whereas zinc-free LD showed almost no activity. This is because the positively charged Zn^{2+} ions in ZnO undergo electrostatic attraction to the negatively charged phospholipid bilayer on the bacterial surface. The interaction alters membrane permeability, disrupts the native charge balance of the cell wall, and causes leakage of essential intracellular components such as electrolytes,

Table 3 Fatigue test results

	Sample1	Sample 2	Sample 3	Sample 4	Sample 5	Sample 6	Sample 7	Sample 8	Sample 9	Sample 10
FFL (N)	232.2	225.8	231.5	211.6	218.5	232.2	230.8	215.2	226.3	234.1
Number of cycles until failure (NCF)	51,332	50,524	51,370	49,735	50,804	51,440	51,432	50,040	51,298	51,501

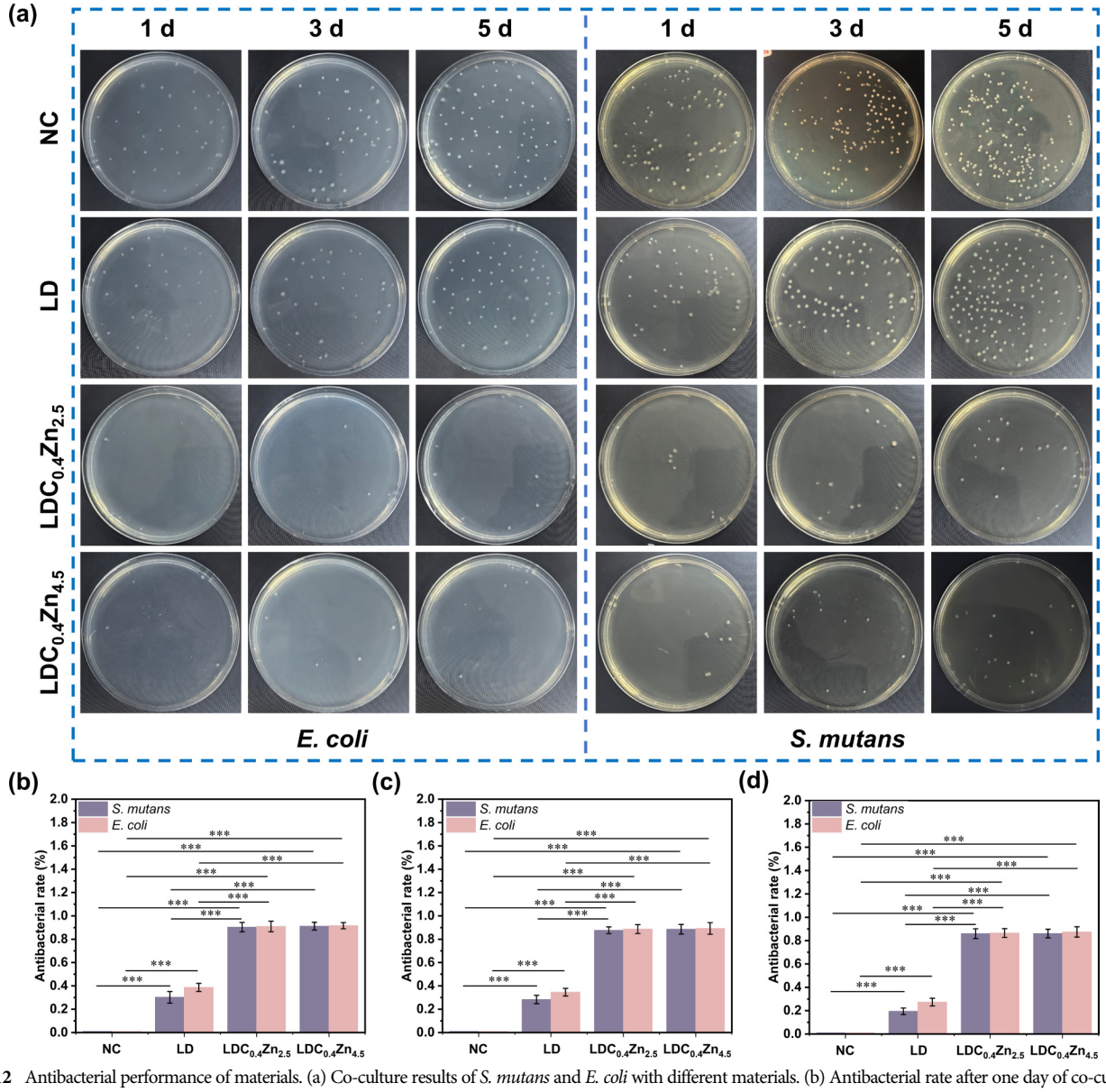

Fig. 12 Antibacterial performance of materials. (a) Co-culture results of *S. mutans* and *E. coli* with different materials. (b) Antibacterial rate after one day of co-culture. (c) Antibacterial rate after three days of co-culture. (d) Antibacterial rate after five days of co-culture. (*** represents $P < 0.001$ ($n = 3$)).

proteins, and nucleic acids, ultimately leading to cell lysis and death [52]. Moreover, in the moist oral environment, ZnO can adsorb oxygen via surface oxygen vacancies and catalyze its conversion into reactive oxygen species (ROS), which then damage essential cellular components and cause bacterial death [52,53]. By the third and fifth days, the antibacterial rate of the ZnO-doped material dropped to approximately 87% and 86%, respectively. This decline was attributed to the gradual accumulation of bacterial debris, proteins, and other impurities on the ceramic surface, which formed a "shielding layer". This layer impeded direct contact between Zn^{2+} ions and the bacteria and hindered the photocatalytic reactions of Zn^{2+}, ultimately reducing the antimicrobial efficacy. Nevertheless, after five days, the antibacterial rate remained stable above 85%, indicating that the material could sustain its antimicrobial activity. It was also noteworthy that the inhibition rate of $LDC_{0.4}$ $Zn_{4.5}$ was consistently slightly higher than that of $LDC_{0.4}Zn_{2.5}$, a consequence of its greater ZnO content. Moreover, for any given material, the efficacy against *E. coli* was marginally superior to that against *S. mutans*, probably owing to differences in the structure of their cell walls [54].

4 Conclusions

Guided by light scattering theory and functional requirements, this study successfully developed a novel design methodology for lithium silicate/C/ZnO composite powders to address the critical challenges of poor forming accuracy and inadequate antibacterial activity in lithium silicate glass-ceramic dentures fabricated via vat photopolymerization 3D printing. The main conclusions are summarized as follows:

(1) This innovative composite powder design concurrently improved interlayer bonding and enhanced the printing precision of lithium silicate glass-ceramics by 91.72%. The synergistic combination of C and ZnO enabled optimal control over the optical properties of the slurry. While C confined the light scattering to enhance printing accuracy, ZnO moderated its excessive absorption to ensure sufficient curing depth and robust interlayer bonding. This balanced approach successfully improved both printing accuracy and curing quality, validating the composite strategy for tailoring optical parameters.

(2) The synergistic interaction between C and ZnO significantly reinforced the mechanical properties of the 3D-printed lithium silicate glass-ceramics, resulting in a 43.1% increase in flexural strength to 297.28 MPa and an 8.4% improvement in fracture toughness to 3.74 MPa·$m^{1/2}$. This enhancement is attributed to the multifunctional role of ZnO, which increased the curing depth to ensure robust interlayer adhesion, promoted sintering densification, and generated beneficial compressive stresses.

(3) The incorporation of ZnO markedly enhanced the antibacterial efficacy of lithium disilicate glass-ceramics, which exhibited sustained antibacterial efficacy against both *E. coli* and *S. mutans*, satisfying the clinical requirements for antibacterial functionality in dental restorative applications.

Acknowledgements

This study was supported by the National Natural Science Foundation of China (Nos. 52475263 and 52175408), Shandong Higher Education Youth Innovation and Technology Support Program (No. 2023KJ110), University of Jinan Disciplinary Cross-Convergence Construction Project 2024 (No. XKJC-202406), and Taishan Scholar Engineering Special Funding (2022–2027).

Author contributions

Fan Zhang: writing – original draft preparation. Yujun Zhang: resources and methodology. Junfeng Kang: validation. Shouren Wang: formal analysis. Zhen Xiao: writing – review and editing. Xiuli Fu: resources and methodology. Gaoqi Wang: writing – original draft preparation and funding acquisition.

Availability of data and materials

The data that support the findings of this study are available from the corresponding author upon reasonable request.

Competing interests

The authors have no competing interests to declare that are relevant to the content of this article.

References

[1] Fu L, Engqvist H, Xia W. Glass–ceramics in dentistry: A review. *Materials* 2020, **13**: 1049.
[2] Kelly JR, Benetti P. Ceramic materials in dentistry: Historical evolution and current practice. *Aust Dent J* 2011, **56**: 84–96.
[3] Niu E, Agustin M, Douglas RD. Color match of machinable lithium disilicate ceramics: Effects of foundation restoration. *J Prosthet Dent* 2013, **110**: 501–509.
[4] Li K, Kou HM, Ning CQ. Sintering and mechanical properties of lithium disilicate glass-ceramics prepared by sol-gel method. *J Non-Cryst Solids* 2021, **552**: 120443.
[5] Baumgartner S, Gmeiner R, Schönherr JA, *et al.* Stereolithography-based additive manufacturing of lithium disilicate glass ceramic for dental applications. *Mat Sci Eng C—Mater* 2020, **116**: 111180.
[6] Diao Q, Zeng Y, Chen JM. The applications and latest progress of ceramic 3D printing. *Addit Manuf Front* 2024, **3**: 200113.
[7] Giordano R. Materials for chairside CAD/CAM-produced restorations. *J Am Dent Assoc* 2006, **137**: 14S–21S.
[8] Wu HL, Guo AF, Kong DK, *et al.* Additive manufacturing of bionic layered ceramic-metal composites for enhanced toughness and damage resistance. *Virtual Phys Prototy* 2025, **20**: 2443102.
[9] Yang WL, Guo AF, Sheng XL, *et al.* Preparation of 316L stainless steel/WC gradient layered structures with excellent strength–elongation synergy using laser powder bed fusion. *J Manuf Process* 2025, **133**: 692–704.
[10] He RJ, Zhou NP, Zhang KQ, *et al.* Progress and challenges towards additive manufacturing of SiC ceramic. *J Adv Ceram* 2021, **10**: 637–674.
[11] Alves MFRP, dos Santos C, Duarte I, *et al.* Complex shapes of lithium disilicate glass-ceramics developed by material extrusion. *Addit Manuf* 2024, **80**: 103973.
[12] Wu HL, Guo AF, Kong DK, *et al.* Preparation of Bouligand biomimetic ceramic composites and the effect of different fiber orientations on mechanical properties. *J Manuf Process* 2024, **132**: 789–801.
[13] Marsico C, Carpenter I, Kutsch J, *et al.* Additive manufacturing of lithium disilicate glass-ceramic by vat polymerization for dental appliances. *Dent Mater* 2022, **38**: 2030–2040.
[14] Chen RF, Duan WY, Wang G, *et al.* Surface modification of Si_3N_4 powder and its effect on digital light processing. *Bull Chin Ceram Soc* 2021, **40**: 1957–1964. (in Chinese)
[15] Qian CC, Hu KH, Li JH, *et al.* The effect of light scattering in stereolithography ceramic manufacturing. *J Eur Ceram Soc* 2021, **41**: 7141–7154.
[16] Jang KJ, Kang JH, Sakthiabirami K, *et al.* Evaluation of cure depth and geometrical overgrowth depending on zirconia volume fraction using digital light processing. *J Nanosci Nanotechno* 2019, **19**: 2154–2157.
[17] Nagrath M, Sikora A, Graca J, *et al.* Functionalized prosthetic interfaces using 3D printing: Generating infection-neutralizing prosthesis in dentistry. *Mater Today Commun* 2018, **15**: 114–119.

[18] Yang BB, Wang SR, Wang GQ, *et al.* Mechanical properties and wear behaviors analysis of fluorapatite glass-ceramics based on stereolithography 3D printing. *J Mech Behav Biomed* 2021, **124**: 104859.
[19] Su RY, Chen JY, Zhang XQ, *et al.* Accuracy controlling and mechanical behaviors of precursor-derived ceramic SiOC microlattices by projection micro stereolithography (PμSL) 3D printing. *J Adv Ceram* 2023, **12**: 2134–2147.
[20] Shen YR, Sun Y, Jin BC, *et al.* Effect of debinding and sintering profile on the optical properties of DLP-3D printed YAG transparent ceramic. *Ceram Int* 2022, **48**: 21134–21140.
[21] He N, Wang XN, Shi LY, *et al.* Photoinhibiting via simultaneous photoabsorption and free-radical reaction for high-fidelity light-based bioprinting. *Nat Commun* 2023, **14**: 3063.
[22] Wang GQ, Shen W, Li YK, *et al.* Improved mechanical performance and forming accuracy of fluorapatite glass-ceramics manufactured using vat photopolymerization with the addition of zirconia. *Addit Manuf* 2023, **74**: 103718.
[23] Pasquet J, Chevalier Y, Couval E, *et al.* Antimicrobial activity of zinc oxide particles on five micro-organisms of the Challenge Tests related to their physicochemical properties. *Int J Pharmaceut* 2014, **460**: 92–100.
[24] Pasquet J, Chevalier Y, Couval E, *et al.* Zinc oxide as a new antimicrobial preservative of topical products: Interactions with common formulation ingredients. *Int J Pharmaceut* 2015, **479**: 88–95.
[25] Li JH, Fan HT, Li H, *et al.* Recent advancements in the surface modification of additively manufactured metallic bone implants. *Addit Manuf Front* 2025, **4**: 200195.
[26] Liu YL, Wang RL, Li N, *et al.* Preparation of zinc oxide mesocrystal filler and the properties of dental composite resins. *J Inorg Mater* 2019, **34**: 1077–1084.
[27] Dai ZX, An JL, Huang XF. Arginine-loaded mesoporous silica nanoparticles modified 3D-printed nanocomposite denture base resin with improved mechanical and antimicrobial properties. *BMC Oral Health* 2025, **25**: 1205.
[28] Zhang Y, Hu M, Zhang W, *et al.* Homology of selenium (Se) and tellurium (Te) endow the functional similarity of Se-doped and Te-doped mesoporous bioactive glass nanoparticles in bone tissue engineering. *Ceram Int* 2022, **48**: 3729–3739.
[29] Westbeek S, van Dommelen JAW, Remmers JJC, *et al.* Influence of particle shape in the additive manufacturing process for ceramics. *Comput Math Appl* 2019, **78**: 2360–2376.
[30] Westbeek S, Remmers JJC, van Dommelen JAW, *et al.* Multi-scale process simulation for additive manufacturing through particle filled vat photopolymerization. *Comp Mater Sci* 2020, **180**: 109647.
[31] Laidani N, Bartali R, Gottardi G, *et al.* Optical absorption parameters of amorphous carbon films from Forouhi–Bloomer and Tauc–Lorentz models: A comparative study. *J Phys-Condens Mat* 2008, **20**: 015216.
[32] Bolarinwa HS, Onuu MU, Fasasi AY, *et al.* Determination of optical parameters of zinc oxide nanofibre deposited by electrospinning technique. *J Taibah Univ Sci* 2017, **11**: 1245–1258.
[33] Osmanlic F, Wudy K, Laumer T, *et al.* Modeling of laser beam absorption in a polymer powder bed. *Polymers* 2018, **10**: 784.
[34] Tavassoli Hojati S, Alaghemand H, Hamze F, *et al.* Antibacterial, physical and mechanical properties of flowable resin composites containing zinc oxide nanoparticles. *Dent Mater* 2013, **29**: 495–505.
[35] Sergi R, Bellucci D, Salvatori R, *et al.* Zinc containing bioactive glasses with ultra-high crystallization temperature, good biological performance and antibacterial effects. *Mat Sci Eng C—Mater* 2019, **104**: 109910.
[36] Chen JY, Su RY, Zhai XF, *et al.* Improving the accuracy of stereolithography 3D printed Al_2O_3 microcomponents by adding photoabsorber: Fundamentals and experiments. *J Mater Res Technol* 2023, **27**: 757–766.
[37] Ma JF, Zhou X, Ye ZQ, *et al.* β-spodumene-doped lithium disilicate glass-ceramics via additive manufacturing for dental applications. *J Mater Sci Technol* 2026, **247**: 289–301.
[38] Zhou X, Yao YX, Tong X, *et al.* Additively manufactured lithium disilicate glass-ceramics for dental applications: Role of heat treatment on densification, microstructural evolution, and strengthening-toughening. *J Eur Ceram Soc* 2025, **45**: 117187.
[39] Li CL, Wang GQ, Hao ML, *et al.* Synergistic material-process optimization enables high-performance silicon carbide ceramic fabrication via vat photopolymerization. *J Eur Ceram Soc* 2025, **45**: 117714.
[40] Coldea A, Swain MV, Thiel N. Mechanical properties of polymer-infiltrated-ceramic-network materials. *Dent Mater* 2013, **29**: 419–426.
[41] Nastic A, Merati A, Bielawski M, *et al.* Instrumented and Vickers indentation for the characterization of stiffness, hardness and toughness of zirconia toughened Al_2O_3 and SiC armor. *J Mater Sci Technol* 2015, **31**: 773–783.
[42] Liu Y, Zhan LN, Wen L, *et al.* Effects of particle size and color on photocuring performance of Si_3N_4 ceramic slurry by stereolithography. *J Eur Ceram Soc* 2021, **41**: 2386–2394.
[43] Bai Y, Peng L, Zhu QS. The preparation of the lithium disilicate glass-ceramic with high translucency. *J Non-Cryst Solids* 2017, **457**: 129–134.
[44] Simba BG, Ribeiro MV, Suzuki PA, *et al.* Mechanical properties of lithium metasilicate after short-term thermal treatments. *J Mech Behav Biomed* 2019, **98**: 179–186.
[45] German RM. Rheological model for viscous flow densification during supersolidus liquid phase sintering. *Sci Sinter* 2006, **38**: 27–40.
[46] Yao JH, Elder KR, Guo H, *et al.* Theory and simulation of Ostwald ripening. *Phys Rev B* 1993, **47**: 14110–14125.
[47] Xu XL, Wang P, Qi ZM, *et al.* Formation mechanism of Zn_2SiO_4 crystal and amorphous SiO_2 in ZnO/Si system. *J Phys-Condens Mat* 2003, **15**: L607–L613.
[48] Chen XP, Xiang ZX, Song XF, *et al.* Machinability: Zirconia-reinforced lithium silicate glass ceramic versus lithium disilicate glass ceramic. *J Mech Behav Biomed* 2020, **101**: 103435.
[49] Serbena FC, Zanotto ED. Internal residual stresses in glass-ceramics: A review. *J Non-Cryst Solids* 2012, **358**: 975–984.
[50] Alves MFRP, Ferrandez-Montero A, Ferrari B, *et al.* Manufacturing of lithium disilicate glass-ceramics by Vat-photopolymerization of water-based photocurable suspensions. *Open Ceram* 2025, **21**: 100742.
[51] Buser R, Dönmez MB, Hoffmann M, *et al.* Fatigue behavior and reliability of pressed lithium disilicate ceramics compared to 5Y-TZP zirconia under different loading protocols. *Dent Mater* 2025, **41**: 134–140.
[52] Sirelkhatim A, Mahmud S, Seeni A, *et al.* Review on zinc oxide nanoparticles: Antibacterial activity and toxicity mechanism. *Nano-Micro Lett* 2015, **7**: 219–242.
[53] Yuqing F, Zhang SH, Peng RN, *et al.* Durable antimicrobial microstructure surface (DAMS) enabled by 3D-printing and ZnO nanoflowers. *Langmuir* 2025, **41**: 3027–3032.
[54] Söderberg TA, Sunzel B, Holm S, *et al.* Antibacterial effect of zinc oxide *in vitro*. *Scand J Plast Recons* 1990, **24**: 193–197.